

See discussions, stats, and author profiles for this publication at: <https://www.researchgate.net/publication/272202691>

Chemical and Electronic Structure Characterization of Lead Halide Perovskites and Stability Behavior under Different Exposures—A Photoelectron Spectroscopy Investigation

ARTICLE *in* CHEMISTRY OF MATERIALS · FEBRUARY 2015

Impact Factor: 8.35 · DOI: 10.1021/acs.chemmater.5b00348

CITATIONS

11

READS

295

7 AUTHORS, INCLUDING:



Bertrand Philippe

Uppsala University

16 PUBLICATIONS 253 CITATIONS

[SEE PROFILE](#)



Byung-wook Park

Ulsan National Institute of Science and Techn...

25 PUBLICATIONS 259 CITATIONS

[SEE PROFILE](#)



Erik M. J. Johansson

Uppsala University

72 PUBLICATIONS 1,708 CITATIONS

[SEE PROFILE](#)

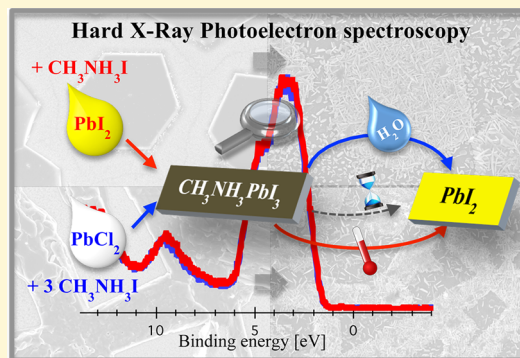
Chemical and Electronic Structure Characterization of Lead Halide Perovskites and Stability Behavior under Different Exposures—A Photoelectron Spectroscopy Investigation

Bertrand Philippe,^{*,†} Byung-Wook Park,[‡] Rebecka Lindblad,[†] Johan Oscarsson,[†] Sareh Ahmadi,[†] Erik M. J. Johansson,[‡] and Håkan Rensmo^{*,†}

[†]Department of Physics and Astronomy, Uppsala University, Box 516, SE-75121, Uppsala, Sweden

[‡]Department of Chemistry—Ångström Laboratory, Uppsala University, Box 523, SE-75121 Uppsala, Sweden

ABSTRACT: The past few years, two perovskite materials have attracted much attention in the solar cell community: $\text{CH}_3\text{NH}_3\text{PbI}_3$ and $\text{CH}_3\text{NH}_3\text{PbI}_{3-x}\text{Cl}_x$. While these materials are usually characterized using their structure (via X-ray diffraction (XRD)) and performance within solar cell communities, not so much attention has been devoted to their surface chemical composition and, specifically, the surface composition. Photoelectron spectroscopy (PES) can easily fulfill this task, and, in addition to chemical information, PES provides an overall picture of the electronic structure of the perovskite and its relation to mesoporous TiO_2 when studied with hard X-rays. In this work, $\text{CH}_3\text{NH}_3\text{PbI}_3$ and $\text{CH}_3\text{NH}_3\text{PbI}_{3-x}\text{Cl}_x$ have been compared with each other and also to $\text{CH}_3\text{NH}_3\text{PbCl}_3$, and it appears that, despite very different morphologies and kinetics of formation, the two former materials present a very similar electronic structure and chemical composition (i.e., no chlorine is observed in the final $\text{CH}_3\text{NH}_3\text{PbI}_{3-x}\text{Cl}_x$ materials). Nevertheless, chlorine is very important during the preparation, because it affects the formation of crystalline $\text{CH}_3\text{NH}_3\text{PbI}_3$. We have also exposed the classical $\text{CH}_3\text{NH}_3\text{PbI}_3$ to various environments, such as water, temperature, and long-time storage in air and argon, and followed changes of the surface composition with PES. The main result of the different exposures is that the perovskite is decomposed into PbI_2 , but an important point is that this degradation seems to occur already at 100 °C and is not only related to large humidity. Indeed, even in an inert atmosphere such as argon, a slow degradation to PbI_2 is observed. The results obtained are crucial for a better understanding of this material and will help to improve not only the post-conditioning of the cells but also their synthesis.



1. INTRODUCTION

The use of organic–inorganic metal halide perovskites as light absorbers is one of the most significant breakthroughs in the field of solar cells in the past five years.^{1–4} The classical perovskite structure is a well-established reference in crystallography; it presents the general chemical formula ABX_3 , with A and B being two cations and X being an anion. Methylammonium lead halide ($\text{CH}_3\text{NH}_3\text{PbX}_3$) belongs to this family, with A = CH_3NH_3^+ , B = Pb^{2+} , and X is a halogen anion (e.g., I^- , Br^- , Cl^- , or a mixture of these elements) and constitutes the system that has attracted so much attention since 2012 in the solar cell community.

The recent breakthrough was largely initiated in 2009 when Kojima et al.⁵ used both $\text{CH}_3\text{NH}_3\text{PbI}_3$ and $\text{CH}_3\text{NH}_3\text{PbBr}_3$ as visible-light sensitizers on TiO_2 in traditional configurations. Efficiencies of 3.81% and 3.13% were reached respectively; however, the stability was very poor, mainly due to the use of a liquid electrolyte. This problem was partly solved when introducing the perovskite in solid-state dye-sensitized solar cells (ssDSSCs).

The current revolution exploded in 2012, when $\text{CH}_3\text{NH}_3\text{PbI}_3$ was directly coupled to a solid hole conductor (spiro-OMeTAD) on mesoporous TiO_2 , reaching an efficiency of 9.7%.⁶ Almost in parallel, a mixed halide perovskite described as $\text{CH}_3\text{NH}_3\text{PbI}_2\text{Cl}$ reported shortly afterward by Lee et al. and gave an efficiency of 10.9% when coated on mesoporous alumina (Al_2O_3).⁷ Since this point, the race toward high efficiency has been quickly developing and solid-state solar cells based on the organic–inorganic metal halide perovskite with efficiencies of <15% have been reported;^{8,9} in addition, Jeon et al. (from the Korean Research Institute of Chemical Technology (KRICT)) recently reported an average efficiency of 18.4%, using $(\text{FAPbI}_3)_{0.85}(\text{MAPbBr}_3)_{0.15}$.¹⁰ This material has established the current record of a 20.1% efficiency cell certified by the U.S. National Renewable Energy Laboratory. Development and improvement of the “perovskite” devices has been attained using different approaches, such as modifying the

Received: December 8, 2014

Revised: February 12, 2015

nature of the halide,^{11,12} the metal,¹³ or the cation group^{14,15} of the materials, as well as the development and optimization of novel fabrication/deposition techniques.^{16–19} The different strategies used are widely reported in recent reviews.^{20,21} In parallel to this development in perovskite solar cell efficiency, more fundamental^{22–26} and computational^{27,28} studies emerged to highlight the charge separation/transfer/recombination mechanisms of these materials. Moreover, to replace the key materials in the more established dye sensitized solar cells another important issues must be addressed: how external conditions affect the stability and structure of these perovskite materials.

In the current paper, we explore how X-ray-based spectroscopy methods can be used to address this question and specifically the effect on the material surface/interface structure. We initially focus on $\text{CH}_3\text{NH}_3\text{PbI}_3$ and the material referred to as the mixed lead halide $\text{CH}_3\text{NH}_3\text{PbI}_{3-x}\text{Cl}_x$. Both materials were synthesized using a dimethyl sulfoxide/dimethylformamide (DMSO:DMF) mixture as solvent. A previous work of our group focused on the structural aspect of these two perovskite materials.²⁹

In the first part of the present paper, we emphasize on the chemical comparison of these two systems, particularly the role of chlorine. The effect of chlorine on the chemical composition of the perovskite phase remains a controversial question that has not been truly solved. This issue is well-illustrated by the evolution of the notation used to refer to this phase, from the first suggested $\text{CH}_3\text{NH}_3\text{PbI}_2\text{Cl}$ to the $\text{CH}_3\text{NH}_3\text{PbI}_{3-x}\text{Cl}_x$ currently used. A survey of the literature already suggests very low chloride incorporation into the perovskite film after the annealing. Supported by DFT calculations, in 2013, Colella et al. noted that only a low concentration of chlorine (below 3%–4%) could be included in the iodine-based perovskites, but this doping significantly improved the charge transport of the material.³⁰ They then suggest that chlorine was located at the interface between the perovskite and TiO_2 by using angle-resolved XPS and calculations.³¹ This doping effect was also reported by Edri et al. on the analogous $\text{CH}_3\text{NH}_3\text{PbBr}_{3-x}\text{Cl}_x$ compared to $\text{CH}_3\text{NH}_3\text{PbBr}_3$; however, no chlorine could be detected by EDS, and a minor chlorine presence (just a few percent) was detected by XPS, according to the authors.³² A total absence of chlorine was also evoked by Dualeh et al., which suggested a sublimation of excess organic $\text{CH}_3\text{NH}_3\text{Cl}$ during the annealing step, the result of which is supported by XRD data.³³ A slightly more-complex reaction mechanism also leading to the release of gaseous $\text{M}\text{A}\text{Cl}$ was proposed by Yu et al.³⁴ The release of $\text{M}\text{A}\text{Cl}$ was directly observed by Unger et al.,³⁵ and a white deposit on a petri dish covering the sample during annealing was observed and characterized as $\text{M}\text{A}\text{Cl}$ by XRD. Less than 1% chlorine was detected in these last two works. Dar et al. suggested that the detected chlorine is most likely from a PbCl_2 residual.³⁶

Electronic structure and determination of the energy band alignment are also important parameters in the community. Mosconi et al. have shown, by calculation, that similar band gaps were obtained for $\text{CH}_3\text{NH}_3\text{PbI}_3$ and $\text{CH}_3\text{NH}_3\text{PbI}_{3-x}\text{Cl}_x$.³⁷ These similarities were confirmed later by Schultz et al. by UPS and IPES spectroscopies³⁸ and reported an energy level diagram of the perovskite versus TiO_2 .

In the second part, the behavior of these materials under certain conditions (such as water exposure, heat treatment, and time) is investigated. So far, instability and degradation of the perovskite phase have been studied mainly by XRD

techniques.^{39–41} In comparison, photoelectron spectroscopy (PES) can give both qualitative and quantitative chemical information independent of the crystallinity of the material investigated.

2. EXPERIMENTAL DETAILS

2.1. Sample Preparation: $\text{CH}_3\text{NH}_3\text{PbI}_3$, $\text{CH}_3\text{NH}_3\text{Pb}_{3-x}\text{Cl}_x$, and $\text{CH}_3\text{NH}_3\text{PbCl}_3$. The perovskite materials and their precursors were prepared following the procedure described in a previous paper;²⁹ the main steps of the preparation are summarized below. A 1.5 M $\text{CH}_3\text{NH}_3\text{PbI}_3$ perovskite precursor solution was formed from an equimolar mixture of $\text{CH}_3\text{NH}_3\text{I}$ and PbI_2 in a solvent mixture of dimethylformamide (DMF) and dimethyl sulfoxide (DMSO) (DMF/DMSO = 7:3 (v:v)). First, the metal halide compound was completely dissolved in the solvent mixture on a hot plate at 70–80 °C; $\text{CH}_3\text{NH}_3\text{I}$ was then added, giving a homogeneous yellow solution after 2 h.

$\text{CH}_3\text{NH}_3\text{PbI}_{3-x}\text{Cl}_x$ perovskite precursor solution was prepared by mixing a 3:1 ratio of $\text{CH}_3\text{NH}_3\text{I}$ (4.5 M) and PbCl_2 (1.5 M) in the same solvent (DMF:DMSO, 7:3). The $\text{CH}_3\text{NH}_3\text{PbCl}_3$ material was prepared after mixing of an equimolar ratio of $\text{CH}_3\text{NH}_3\text{Cl}$ and PbCl_2 in DMSO (1.5M) to get a better solubility of the metal halide compounds.

The $\text{CH}_3\text{NH}_3\text{I}$ and $\text{CH}_3\text{NH}_3\text{Cl}$ precursors were synthesized as described in ref 42.

TiO_2 nanoparticles were spin-coated on fluorine-doped tin oxide (FTO) glass at 3500 rpm for 30 s using a TiO_2 paste from Dyesol (18NR-T, 100% anatase, particle size ca. 20 nm). The TiO_2 paste was prepared by diluting the Dyesol paste with ethanol in a 1:3 (w:w) ratio. The TiO_2 /FTO substrate was annealed on a hot plate at 550 °C for 30 min. The film thickness was estimated to be ~650 nm (± 80 nm) by SEM.

The organic–inorganic lead halide perovskite precursor solutions were filtered through a PVDF syringe filter (Whatman, 0.45 μm pore) and then spin-coated in ambient air onto the TiO_2 /FTO substrate at 1500 rpm for 30 s, followed by annealing on a hot plate at 120 °C for 10 min ($\text{CH}_3\text{NH}_3\text{PbI}_3$) or 1 h ($\text{CH}_3\text{NH}_3\text{PbI}_{3-x}\text{Cl}_x$) in a dry air box (relative humidity (rh) of 10%). The samples used for the time evolution were spin-coated and annealed directly inside an argon-filled glovebox. The annealing time reported corresponds to the time required to observe the color changes of the sample surface from a deep yellow to brown. The difference in annealing time already suggests that the kinetics of formation of these two materials is different. The $\text{CH}_3\text{NH}_3\text{PbCl}_3$ material presents a white color. The deposition process described above is referred to as a one-step method. Hereafter, in this paper, the methylammonium group CH_3NH_3^+ will be denoted as MA.

After the annealing, all the samples were stored in an argon-filled glovebox ($\text{O}_2 < 1$ ppm, $\text{H}_2\text{O} < 1$ ppm) and transferred to the synchrotron facility in a container that also was filled with argon gas, to minimize moisture contamination, if not stated otherwise. The sample used for the heating procedure was deposited on a silicon wafer instead of FTO for better heat transfer through the substrate. Two or 3 days were spent between the sample preparation and the PES analysis, unless stated otherwise.

2.2. Post-Treatments: Water Exposure, Time Evolution, And Heating Procedures. The water exposure on MAPbI_3 and $\text{MAPbI}_{3-x}\text{Cl}_x$ was performed by putting a single drop of deionized (DI) water on a tilted perovskite/ TiO_2 /FTO sample and then allowing it to dry in air for 2 h. A reaction was

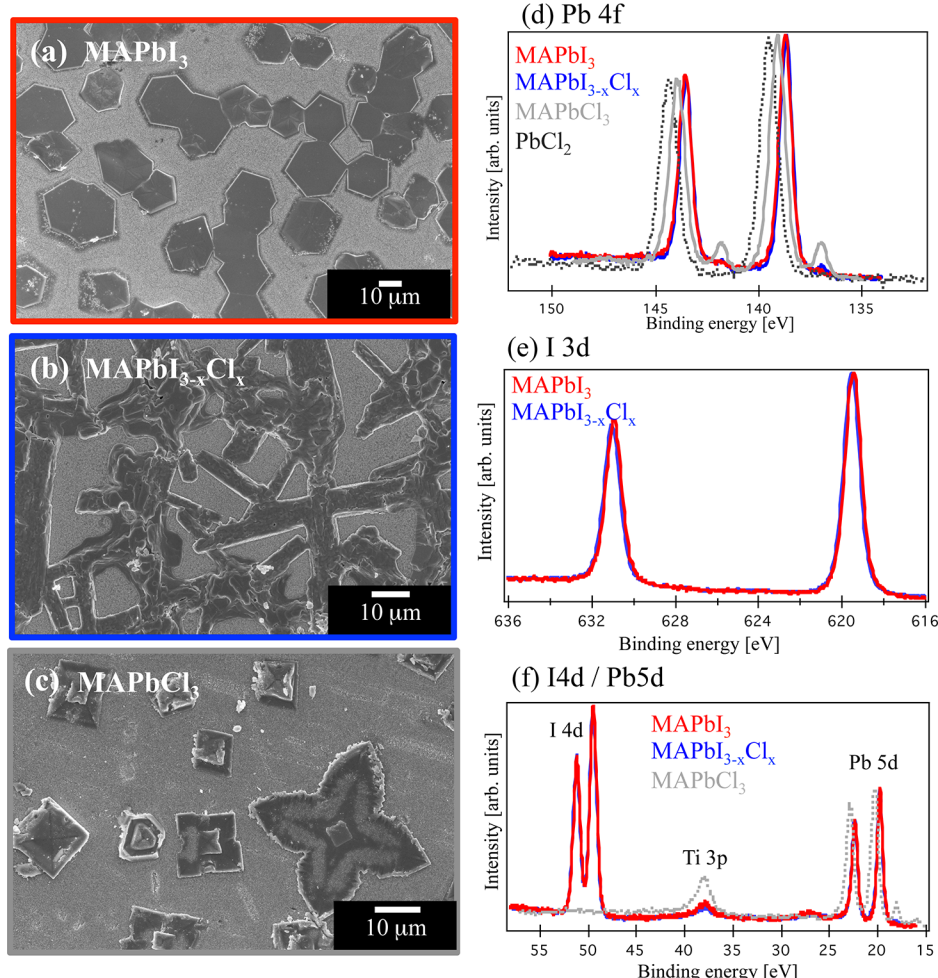


Figure 1. Top-view SEM images of (a) the MAPbI₃ (red frame), (b) MAPbI_{3-x}Cl_x (blue frame), and (c) MAPbCl₃ (gray frame) materials deposited on a TiO₂/FTO substrate. (Horizontal scale bars = 10 mm.) Also shown are (d) Pb 4f spectra, (e) I 3d spectra, and (f) Pb 5d/I 4d spectra of MAPbI₃ (red solid line), MAPbI_{3-x}Cl_x (blue solid line), and MAPbCl₃ (light gray line) recorded with an excitation energy of 4000 eV.

directly observed as a color change after contact with water. The time evolution was performed in two different atmospheres. After an initial XPS measurement, a MAPbI₃ sample was divided into two parts in inert atmosphere. One part was stored in an argon-filled glovebox ($O_2 < 1$ ppm, $H_2O < 1$ ppm), while the second part was kept in ambient air.

Two heating procedures have been carried out on the classical MAPbI₃ material in this paper. They were both performed in the analysis chamber of the spectrometer (in other words, ultra high vacuum environment). During the first procedure, the X-ray beam was switched off when the sample was heated and cooled. The sample was heated for 20 min at 100 °C, cooled to room temperature, and then heated for 20 min at 200 °C. All the PES measurements were done at room temperature before and after the different steps, each time on a fresh spot. In the second heating procedure, the sample was first heated to 100 °C and two successive measurement series were done separated by 150 min. The temperature was then increased to 140 °C, followed by two additional PES measurement series separated by 120 min. Finally, the sample was cooled to room temperature and the last PES measurements were performed. The sample was illuminated by the X-ray beam on the same spot during the entire procedure. The comparison of these two procedures allows us to follow the perovskite degradation with temperature and to distinguish the

degradation of the perovskite caused by heating from possible X-ray damage.

2.3. Hard X-ray Photoelectron Spectroscopy (HAXPES). Hard X-ray PES (HAXPES) was carried out at BESSY II (Helmholtz Zentrum Berlin) at the KMC-1 beamline⁴³ using the HIKE end-station.⁴⁴ This spectroscopy is referred to as hard X-ray photoelectron spectroscopy (HAXPES), as the end-station is provided with a usable photon energy range from 2 keV to 12 keV. The photon energy is selected using a double-crystal monochromator (Oxford-Danfysik) and the photoelectron kinetic energies (KE) were measured using a Model R4000 analyzer (Scienta) optimized for high kinetic energies.

In this work, a photon energy of 4000 eV was used by selecting the first-order light from the Si(311) crystal. A grazing angle was used for the measurement; the angle between the incident beam and the surface of the sample was ~5° (i.e., the sample was facing the analyzer entrance). The pressure in the analysis chamber was ~10⁻⁸ mbar.

Overview spectra and core levels were measured with a pass energy (E_p) of 200 eV. The spectra presented were energy-calibrated versus the Fermi level at zero binding energy, which was determined by measuring a gold plate in electric contact with the sample and setting the Au 4f_{7/2} core level peak to 84.0 eV. The spectra were intensity calibrated using the most intense

peak, if not stated otherwise. Intensity ratios presented between different core levels were calculated from the experimental results after correcting the intensity by the photoionization cross section for each element, using database values.⁴⁵

No charging was observed in the measurements of these different perovskite materials. The charging was controlled by following peak positions and peak shape with variations in light intensity and time. The same procedure was also used to check for X-ray-induced effects. No changes were observed in the spectra reported here; however, some changes were observed after prolonged measurements. These variations will be commented in the Results and Discussion section of this paper. A series of samples was measured and the experimental spectra shown in this work are representative for all measured samples. The observed core level and valence level shifts were similar (within ± 0.1 eV) in all samples, regardless of the method of binding energy calibration: via measurement of the Au 4f core level peak of a gold plate in electric contact with the samples, via measurements of metallic lead or via measurements of a Ti core level from the TiO₂ substrate.

2.4. Energy-Dispersive X-ray Spectroscopy (EDX).

Energy-dispersive X-ray spectroscopy was measured using a liquid-nitrogen-free solid-state spectrometer (Bruker XFlash 4010) with an energy resolution of 133 eV. The instrument is mounted in the vacuum chamber at 45° out of the horizontal plane and also 45° to the beam direction. The EDX data were collected during 40 s at an excitation energy of 5500 eV and over an X-ray fluorescence range of 5–6000 eV.

2.5. Scanning Electron Microscopy (SEM). Scanning electron microscopy (SEM) was performed on a Zeiss microscope (Model Gemini 1550) that had a field-emission (FE) electron source and an in-lens detector for secondary electrons. Images were recorded using a acceleration potential of 10 kV with a working distance of \sim 4 mm.

3. RESULTS AND DISCUSSION

The first part of this paper is focused on the X-ray-based spectroscopic characterization of the two perovskite materials, referred to as MAPbI₃ and MAPbI_{3-x}Cl_x. The MAPbCl₃ material is also characterized for comparison. Spectral differences are expected, as the chemical composition of these three materials is different. Special attention will be devoted to the Cl⁻ atoms and their role in the MAPbI_{3-x}Cl_x perovskite structure, which still is an issue that remains not fully understood. Based on the similarity between the MAPbI₃ and MAPbI_{3-x}Cl_x materials, the latter sections investigating exposure of different environments partly focus on MAPbI₃.

3.1. Characterization of the MAPbI₃ and MAPb_{3-x}Cl_x Materials. A one-step deposition method was used in this work, and the resulting surface morphology of the MAPbI₃, MAPbI_{3-x}Cl_x, and MAPbCl₃ materials deposited onto a mesoporous TiO₂/FTO substrate are presented in the SEM pictures in Figures 1a, 1b, and 1c, respectively. The bright part corresponds to the mesoporous TiO₂ substrate and the dark part corresponds to the organic–inorganic lead halide phase. The island structure observed is typically obtained when a one-step solution-processed deposition is carried out¹⁶ and is in contrast to the more-uniform layer obtained in a two-step process.¹⁸ For a given material, the morphology of these islands is highly dependent on the experimental conditions, e.g., precursor mixing time, annealing time, annealing temperature, etc.^{29,33,46} Among the experimental conditions, it has been showed by Bass et al. that the moisture content during the

perovskite preparation has a tremendous impact by enhancing the crystallinity of CH₃NH₃PbI₃ or CH₃NH₃PbBr₃ perovskite materials.⁴⁷ In our work, SEM images show hexagonal structures for MAPbI₃ samples, whereas for MAPbI_{3-x}Cl_x, a more heterogeneous structure was observed, as presented in Figure 1. MAPbCl₃ exhibited a crystalline structure, which is very different from the other two structures, adopting a flower-like shape. The morphologies of the MAPbI₃ and MAPbI_{3-x}Cl_x are different and have been discussed, from the structural point of view, in previous work.^{29,48} In this context, it is worth remembering that (i) the kinetics of formation of these two phases are very different and (ii) the perovskite formation, which is observed by the color change of the deposited layer (from yellow to brown), occurs in a few minutes for MAPbI₃, while \sim 1 h is needed for MAPbI_{3-x}Cl_x.

From these first observations, it is clear that the use of chlorine (PbCl₂ instead of PbI₂ as metal halide precursor) has a strong impact on the perovskite formation regarding its formation kinetics and its global morphology. Tidhar et al. recently illustrated this crucial role of PbCl₂ in the crystallization process.⁴⁹ However, as described below, the results from photoelectron spectroscopy (HAXPES) show that the differences between MAPbI₃ and MAPbI_{3-x}Cl_x in chemical composition and, thus, the electronic structure are less obvious.

Before commenting on the PES results, it is important to point out that MAPbI₃ and MAPbI_{3-x}Cl_x were prepared on the same day, with the same MAI precursor and solvents batches, and they were stored together under exactly the same conditions and for the same times prior to analysis. Figure 1d shows the Pb 4f spectra of MAPbI₃, MAPbI_{3-x}Cl_x, and MAPbCl₃. The two main peaks observed result from the spin-orbit splitting of the f orbital and are assigned as Pb 4f_{5/2} (141–146 eV region) and Pb 4f_{7/2} (136–141 eV region). The binding energy difference between the 5/2 and 7/2 components is 4.85 eV for the three materials. A small peak at low binding energy (137.0 eV) is also observed for the three materials, because of the presence of Pb⁰; this value is often reported in the literature.^{28,50} The MAPbI₃ sample shows a binding energy of 138.6 eV for the main Pb 4f_{7/2} contribution, corresponding to Pb²⁺, which is in perfect agreement with previous results.²⁸ If we turn to the MAPbCl₃, the Pb 4f_{7/2} peak is located at 139.1 eV and a significant Pb⁰ contribution is also present at 137.0 eV. The 0.5 eV shift of the main peak (Pb²⁺) is expected as a result of the different nature of the halide present in the structure. The spectrum corresponding to the precursor PbCl₂/TiO₂ is represented in this figure, and its Pb 4f_{7/2} peak has a binding energy of 139.5 eV. A binding energy shift of 0.4 eV is thus observed between MAPbCl₃ and PbCl₂. Based on the Pb 4f_{7/2} binding energy difference between MAPbI₃ and MAPbCl₃, the Pb 4f_{7/2} for MAPbI_{3-x}Cl_x could be expected to be somewhere between the two. Nevertheless, the mixed halide sample is perfectly overlapping the MAPbI₃ phase at 138.6 eV, which suggests a very low chlorine content and a similar electronic structure. The metallic lead observed in Figure 1d is present in the samples before the PES measurements and is most likely formed during the preparation of the materials. The intensity of the metallic contribution can vary, depending on the preparation batch. However, the contribution of metallic lead can also increase due to the X-ray exposure, which is further discussed later in this paper.

The I 3d spectra (Figure 1e) confirm the similarities between MAPbI₃ and MAPbI_{3-x}Cl_x, both presenting a single I 3d_{5/2} peak at 619.4 eV with a spin-orbit splitting of 11.5 eV to I

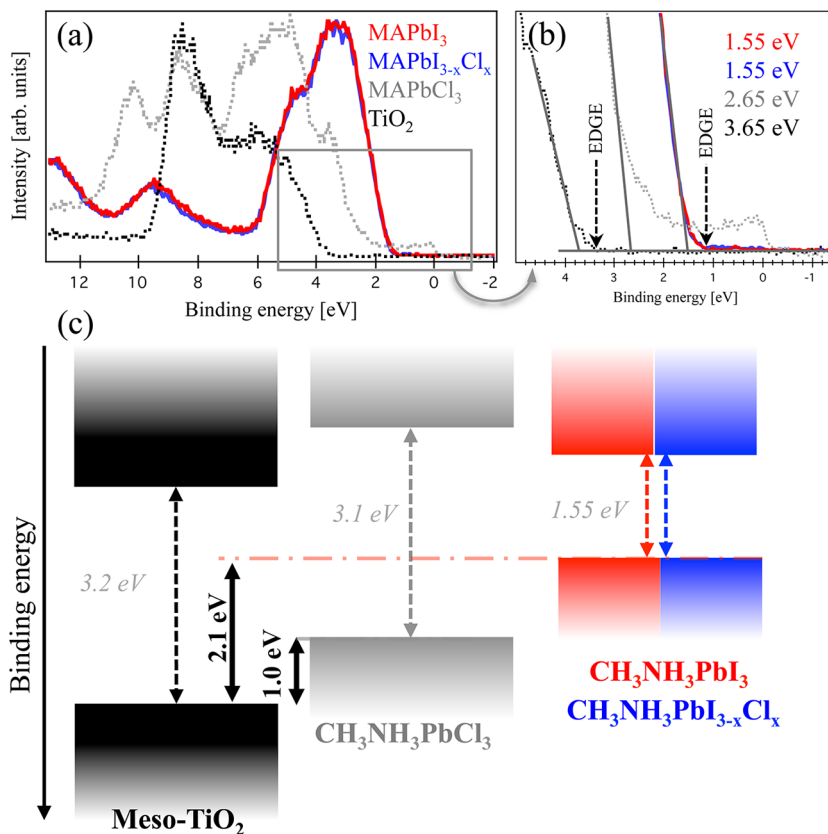


Figure 2. (a) Valence level spectra of the meso-TiO₂ film, MAPbCl₃, MAPbI₃, and MAPbI_{3-x}Cl_x on TiO₂, measured by PES with an excitation energy of 4000 eV in black, gray, red, and blue, respectively. The highest peaks are put to the same height for simple comparison. (b) Expanded view of the valence band. (c) Schematic drawing of the energy level diagram using the intersection of the linear extrapolation shown in panel (b), as well as the optical band gaps (see text).

3d_{3/2}. Figure 1f represents the PES spectra in the 60–15 eV range covering the I 4d core levels (53–48 eV), the Pb 5d core level (25–15 eV), and Ti 3p core level peak (38 eV) from the TiO₂ substrate. The practical advantage of this representation, compared to Figures 1d and 1e, is that information from iodine and lead are displayed in the same spectral range and the relative intensity ratio between Pb and I are measured with a specific probe depth, which can easily be observed without numerous calculations. These spectra have been intensity normalized with respect to the Pb 5d_{5/2} peak intensity. As observed for the Pb 4f_{7/2} core level peak, the Pb 5d_{5/2} core level peaks assigned to MAPbI₃ and MAPbI_{3-x}Cl_x are overlapping with a binding energy of 19.7 eV. The peak of MAPbCl₃ is shifted by +0.5 eV, to 20.2 eV. In the same figure, the I 4d_{5/2} core levels are composed of a single peak at ~49.5 eV for both perovskite materials that contain iodine. If considering the two materials MAPbI₃ and MAPbI_{3-x}Cl_x for $x \neq 0$, the I/Pb ratio should be different, which would result in a difference of the I 4d intensity when normalizing with respect to Pb 5d. Nevertheless, we can see that the I 4d peaks of the two perovskite phases clearly have the same relative intensity, suggesting a similar I/Pb ratio. The calculated ratio value will be presented later in this paper.

The valence band spectra of the meso-TiO₂ and MAPbI₃/TiO₂, MAPbCl₃/TiO₂, and MAPbI_{3-x}Cl_x/TiO₂ interfaces are presented in Figure 2a. The overall shape of the spectral contributions from MAPbI₃ and MAPbI_{3-x}Cl_x are very similar, as could be expected from the core level measurement discussed above and due to the similarity in the lead–iodine

contribution.²⁸ The measured valence structure of MAPbCl₃ and TiO₂ present a completely different electronic structure. An enlarged view of the valence band edge is presented in Figure 2b. Before discussing this further, it is important to notice that the valence band edge of MAPbCl₃ does not decrease to zero intensity and a structure is observed in the 0–2 eV range. This structure results directly from the presence of a noticeable amount of metallic lead in the sample, as mentioned in the discussion of the core level peaks in Figure 1d.

The linear extrapolations drawn in Figure 2 represent a major decrease in the density of states, and this can be used to compare the relative position of the outer valence band. The relative position of the extrapolation for MAPbI₃ and MAPbI_{3-x}Cl_x perovskite materials are at a similar position 2.1 eV from the TiO₂ substrate, in agreement with previous work,²⁸ while the line of MAPbCl₃ is shifted 1.1 eV toward higher binding energies. Although such extrapolations are very common and can be assumed to give a first approximation of the energy level alignment, it is important to realize that a more precise positioning of the valence band edge structure requires a deeper insight into the electronic structure of the solid material including dispersion, energy level character, and cross sections. The latter is sensitive to the X-ray photon energy, and, therefore, the experimental shape may vary in experimental spectra by using low photon energies (UPS) or higher photon energies (e.g., X-ray PES based on Al K α). Another difference of using higher photon energy, compared to UPS, is the increased bulk sensitivity, and, therefore, these measurements are less influenced by surface defects and contaminations.

Moreover, more bulk sensitivity conditions, such as those of hard X-ray photoelectron spectroscopy also enables us to measure the TiO_2 substrate and the perovskite material simultaneously. As an illustration, the difference between the valence band of the perovskite compared to that of TiO_2 was determined to be 1.5 eV by UPS,³⁸ which is quite different from the HAXPES results obtained here or by Lindblad et al. (i.e., 2.1 eV).²⁸ For such a representation, the use of high photon energy appears to be more accurate as both the perovskite and the TiO_2 substrate can be probed at the same time.

As evidenced by Figure 2b, states are found at binding energies lower than the intersection of the linear extrapolation. Based on this structure, an edge position at a binding energy ~ 0.4 eV lower than the intersection is indicated (black arrow) for TiO_2 , as well as MAPbI_3 and $\text{MAPbI}_{3-x}\text{Cl}_x$. For MAPbCl_3 , such estimation was prevented, because of the contribution from the metallic lead. We can note that the binding energy for the indicated edge position has a value close to the bandgap energy of 3.2 eV, which is often used as the value for TiO_2 anatase. Such a procedure supports the notion that the Fermi level of the meso- TiO_2 is very close to the edge of the conduction band.⁵¹ The relative valence band positions for the different perovskite materials and the meso- TiO_2 are summarized together with the reported optical band in a simplified energy diagram (see Figure 2c). An optical band gap of 3.2 eV has been used for TiO_2 , 3.1 eV for MAPbCl_3 , and 1.55 eV for MAPbI_3 and $\text{MAPbI}_{3-x}\text{Cl}_x$.^{4,23,37,52} A diagram such as that given in Figure 2c gives insight into the experimental energy level alignment of these different materials, including the energy matching between the perovskite materials and the TiO_2 , a very significant parameter in a solar cell. At this point, we can also note that the interfacial effects, including charge transfer, affect the relative position. For example, it was shown in a previous study²³ that the position of the Fermi level, relative to the perovskite, was different when measuring on a flat thick perovskite sample, compared to measurements on a thin perovskite layer on mesoporous TiO_2 . Nevertheless, it is clear from these measurements that the MAPbI_3 and $\text{MAPbI}_{3-x}\text{Cl}_x$ samples show very similar energy matching with TiO_2 .

At this point, regarding the PES results of the major constituents comprising MAPbI_3 and $\text{MAPbI}_{3-x}\text{Cl}_x$, we have shown that they have a similar I/Pb intensity ratio and show a very similar electronic structure. PES is a very surface sensitive technique that investigates the first 10 nm of the samples. In a first estimation, it appears clear that the mixed halide perovskite $\text{MAPbI}_{3-x}\text{Cl}_x$ has a very low amount of chlorine, at least in this first 10 nm and, thus, in a first estimation, may be referred to as $\text{MAPbI}_{3-\epsilon}\text{Cl}_\epsilon$, with $\epsilon \approx 0$.

We will now focus directly on the chlorine and its presence on the surface, as well as in the bulk of the sample, by coupling PES and EDX analysis.

Although hard X-ray-based PES is more bulk sensitive in comparison to traditional PES, it still provides information from the top 10 nm of the surface of the materials. The Cl 2p spectra of PbCl_2 (dark gray), MAPbCl_3 (light gray), and $\text{MAPbI}_{3-x}\text{Cl}_x$ (blue) are presented in Figure 3a. These spectra have been intensity normalized vs the Pb 4f peak. The PbCl_2 spectrum clearly contains one contribution assigned to an -1 oxidation state (with Cl 2p_{3/2} at a binding energy of 198.9 eV and spin-orbit splitting of 1.6 eV).⁵³ The Cl 2p_{3/2} level of MAPbCl_3 presents the same overall shape but is shifted toward lower binding energy by 0.4 eV (198.5 eV), we can notice that

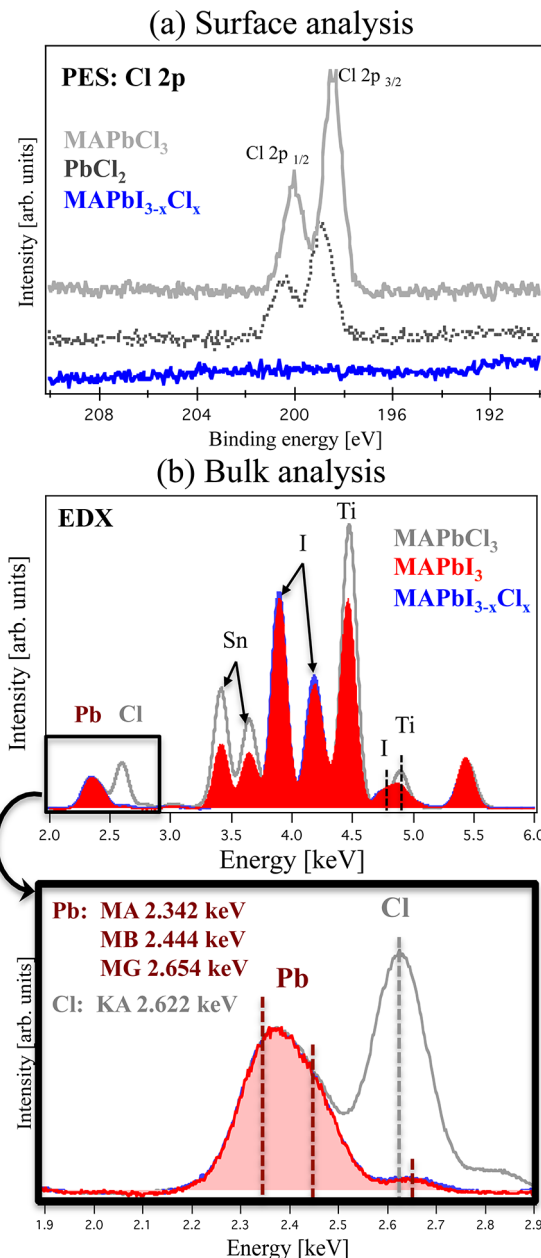


Figure 3. (a) Surface analysis, showing Cl 2p spectra of the MAPbCl_3 (light gray), $\text{MAPbI}_{3-x}\text{Cl}_x$ (blue), and the PbCl_2 precursor (dark gray) samples recorded with an excitation energy of 4000 eV. (b) Bulk analysis, showing EDX spectra of the MAPbI_3 (red), MAPbCl_3 (gray), and $\text{MAPbI}_{3-x}\text{Cl}_x$ (blue) on the 2–6 keV range; the bottom panel shows an expanded view in the ~ 2 –3 keV range.

this shift is similar to the Pb 4f_{7/2} core peak of these same two species and thus that the binding energy difference between Pb and I core levels are very similar for PbCl_2 and MAPbCl_3 . Regarding the mixed halide sample, no Cl peak is detected on the PES spectra. Remembering that the surface sensitivity with the present setup is ~ 10 nm (3 times the mean free path), the results show that no chlorine is present at the outermost surface layers of the samples. From the noise level in the spectra, we estimate the detection limit to be clearly below 1% in this spectra.

Comparisons between perovskite stoichiometry can be made using the relative intensities of the experimental core levels. Such comparisons are rather accurate to follow trends when

comparing materials. Absolute measurements are more difficult and can be sensitive to a range of factors, including geometries between the sample, the detector, the X-ray incident direction, and the light polarization. It is also sensitive to the sample structure including morphology and lateral homogeneity. In the present article, we only use the cross-section from Scofield⁴⁵ to provide some approximate values; as observed in Table 1, reasonable numbers are obtained, although they should not be overinterpreted.

Table 1. Intensity Ratios between Different Core Levels Calculated from Experimental Results

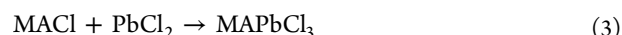
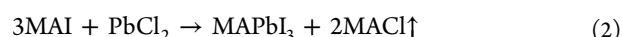
	MAPbI ₃	MAPbI _{3-x} Cl _x	MAPbCl ₃	PbCl ₂
I/Pb intensity ratio	3.3	3.3		
N/Pb intensity ratio	1.1	1.0	1.0	
Cl/Pb intensity ratio		0	2.4	1.4

The absence of chlorine, and, thus, the similarities between MAPbI₃ and MAPbI_{3-x}Cl_x are supported by the values in Table 1. These ratios were calculated using the intensities of the Pb 4f_{7/2}, I 3d_{5/2}, N 1s, and Cl 2p core levels. At this point, it is important to specify that only the main Pb 4f_{7/2} peak (Pb²⁺) was considered in the calculation; the Pb⁰ peak was excluded. The I/Pb ratio is the same for the MAPbI₃ and MAPbI_{3-x}Cl_x sample (3.3) and the N/Pb ratio is 1.0, as expected from the chemical formula. These values confirm the assumption made in Figure 1, despite different synthesis routes: the mixed halide sample does not contain a measurable amount of chlorine in its final structure, i.e. as recently suggested, the notation MAPbI_{3-x}Cl_x should be avoided.⁴ The material is better referred to as MAPbI_{3-ε}Cl_ε, with $\epsilon < 0.01$, because of the detection limits of EDX and XPS or even MAPbI₃, assuming that chlorine is present as PbCl₂, as suggested by Dar et al.³⁶ The experimental Cl/Pb ratio given in Table 1 is 2.4 for the MAPbCl₃ sample (N/Pb = 1) and 1.4 for PbCl₂. At this point, we interpret the deficiency in values to be an inaccuracy in cross-section correction for the Cl 2p orbitals, compared to the N 1s, I 3d, or Pb 4f that may be linked to the angular dependency, rather than a deficiency in chlorine. Similar calculations will be performed in the next part of this paper and it is important to remember that such calculations are mainly used in this work to comment and follow the evolution of the materials, rather than give an absolute value.

In parallel with the HAXPES measurement above, EDX spectroscopy has been carried out on the MAPbI₃, MAPbCl₃, and MAPbI_{3-x}Cl_x samples to get more bulk-sensitive information (several micrometers; see Figure 3b). Indeed, the overall spectra exhibit characteristic peaks of Sn coming from the FTO substrate; therefore, the resulting signal originates from the entire perovskite/TiO₂/FTO sample. These spectra have been normalized to the lead peak at 2.342 keV. The chlorine content is observed in the low-energy area (2–2.8 keV); an enlarged view in this area is provided in Figure 3b (black frame). The Pb contribution is divided into three peaks at 2.342, 2.444, and 2.654 keV. The latter is overlapping with the chlorine peak at 2.622 keV but is clearly observed in MAPbCl₃. Comparing MAPbI_{3-x}Cl_x with MAPbI₃, we can see that no additional features are arising from the mixed halide spectra, suggesting that no measurable amount of chlorine is present in the bulk either. Hence, the lack of chlorine is not only a surface phenomenon.

Via careful comparison of the three different perovskite materials (MAPbI₃, MAPbCl₃, and MAPbI_{3-x}Cl_x) by PES and EDX, we have shown that the organic–inorganic lead mixed halides do not contain any substantial amounts of chlorine in their final structure. However, the presence of chlorine in the synthesis has a strong impact on the structural morphology and on the kinetics of the perovskite formation. The formation is significantly slower with chlorine, which may affect the possibility to control the perovskite formation. Yu et al. gives an interesting explanation to this difference, highlighting the role of chlorine. The two precursor combinations used (MAI/PbCl₂ and MAI/PbI₂) have two very different molar ratios (3:1 and 1:1, respectively). These results show that an initial excess of a MA⁺ is critical to slow the perovskite formation and thus improve the growth of the crystal domains during annealing; chlorine will then allow the removal of MA⁺ in excess via gaseous MACl.³⁴ A decomposition of MACl into HCl and CH₃NH₂ has also been reported.⁴⁸

With the present HAXPES and EDX measurements, we have proof of the absence of chlorine and we can suggest the following reactions for the perovskite formation on the TiO₂ surface, in good agreement with the literature.^{30,33}



The slow kinetics of reaction 2 can also be explained by examining the overall mechanism, where major structural changes occur by breaking all of the Pb–Cl bonds.

The performance obtained with this organic/inorganic lead iodine perovskite have been widely presented in the literature, but the stability remains an important issue prior to full commercialization. The second part of this paper will address the behavior of the sample under three important conditions: humidity, temperature, and time.

3.2. Stability in Contact with Water: MAPbI₃ and MAPbI_{3-x}Cl_x. To simplify the discussion and distinguish the perovskite materials synthesized through PbI₂ or PbCl₂ as precursors, we will continue to refer to MAPbI_{3-x}Cl_x although we have previously shown that no chlorine content could be detected with the X-ray-based tools.

The effect of water on the surface morphology of MAPbI₃ and MAPbI_{3-x}Cl_x deposited on the TiO₂/FTO substrate is shown in the SEM images in Figure 4. For both systems, we can see that the overall shape of the “islands” described is retained, but the structure is completely different after water exposure. The rather-homogeneous smooth materials, several micrometers in size, are divided into smaller thin, flakelike objects (thickness: <1 μm, length: 1–2 μm). The samples presented in Figure 4 have been analyzed before and after contact to water by PES; the results are presented in Figure 5.

The C 1s and N 1s core levels of the MAPbI₃ and MAPbI_{3-x}Cl_x before and after water exposure are reported in Figures 5a and 5b. Before water contact, the C 1s core level of the two perovskite materials is composed of two peaks: the main one, at 286.5 eV, is assigned to the perovskite material CH₃NH₃PbX₃, and the smaller one, at 285 eV, is attributed to common surface contamination. The N 1s core level is composed of a single peak at 402.6 eV assigned to the amine group of the perovskite (CH₃NH₃PbX₃). After contact with water, the carbon and nitrogen contribution from the

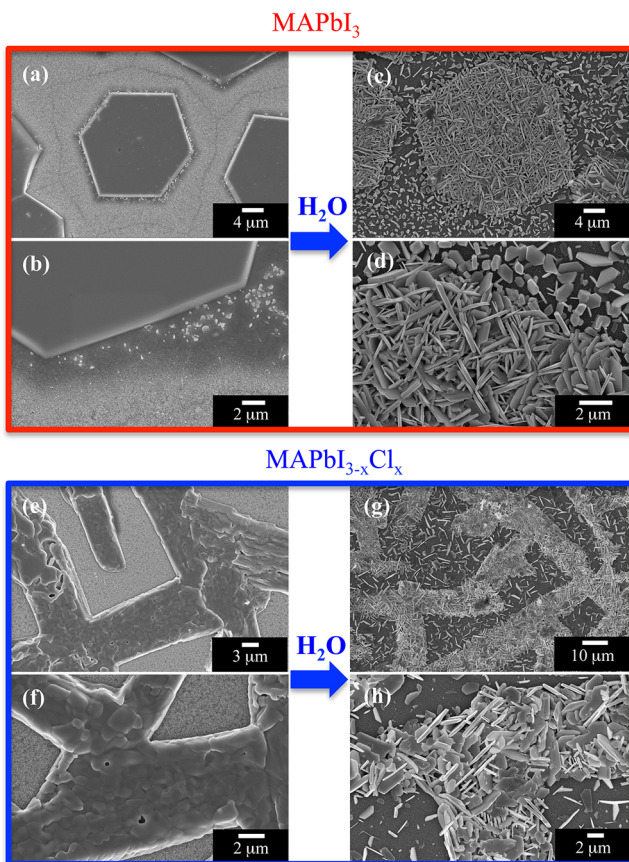
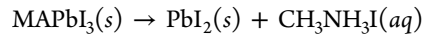


Figure 4. Top-view SEM images of the MAPbI_3 (red frame) materials deposited on a TiO_2/FTO substrate before (panels (a) and (b)) and after (panels (c) and (d)) contact with deionized water. Top-view SEM images of the $\text{MAPbI}_{3-x}\text{Cl}_x$ (blue frame) materials deposited on a TiO_2/FTO substrate before (panels (e) and (f)) and after (panels (g) and (h)) contact with deionized water.

perovskite completely disappears for both systems, showing that the methylammonium group has been totally washed away from the surface. Additional information can be extracted from the evolution of the I 4d/Pb 5d spectral region presented in Figure 5c. These spectra were intensity-normalized vs Pb 5d_{5/2}, and we can see in the enlarged region provided in Figure 5e of the I 4d peak that the spectra of the two perovskite samples behave the same way, after water exposure. The I 4d are shifted toward higher binding energy (+ 0.1 eV), indicating a modification of the chemical environment of I. Second, the I 4d core level peak decreases in intensity, which suggests a modification of the I/Pb ratio. The calculated I/Pb ratios estimated from HAXPES measurements after water exposure are presented in Table 2. For MAPbI_3 and $\text{MAPbI}_{3-x}\text{Cl}_x$, the ratio decreases from 3.3 to 1.9, suggesting a loss of one iodine. This iodine loss can also be observed on the more bulk-sensitive EDX measurement (see Figure 5f). By coupling these data, (i.e., disappearance of an I atom and of the methylammonium group), we can conclude that only PbI_2 remains after water contact and $\text{CH}_3\text{NH}_3\text{I}$ has been dissolved and removed from the perovskite materials. Regarding the picture in Figure 5f, the color change from brown to yellow confirms this complete degradation to PbI_2 and the valence spectra after water exposure presented in Figure 5d are in good agreement with the valence band spectra of a pure PbI_2 phase presented by Lindblad et al.²⁸ In contact with water, the

following reaction can be suggested for both MAPbI_3 and $\text{MAPbI}_{3-x}\text{Cl}_x$ perovskites:



From the PES and EDX spectra, it is clear that both MAPbI_3 and $\text{MAPbI}_{3-x}\text{Cl}_x$ behave in exactly the same way, in the presence of water. The perovskite is completely decomposed and compounds representing $\text{CH}_3\text{NH}_3\text{I}(aq)$ are washed away and give only precipitated PbI_2 as remaining products. If we revisit the SEM photomicrograph presented in Figure 3, it can be seen that the perovskite phase as PbI_2 surrounded by a $\text{CH}_3\text{NH}_3\text{I}$ matrix is removed by water. We also would like to point out that, after water contact, no chlorine was detected on the $\text{CH}_3\text{NH}_3\text{PbI}_{3-x}\text{Cl}_x$ materials in this work, contrary to other work recently presented.⁵⁴

3.3. Stability upon Time in Different Atmospheres of MAPbI_3 . The water exposure of the perovskite presented in the previous part can be considered as extreme and far from the working conditions. In addition, the formation of PbI_2 has been reported in earlier work as the common degradation product under such conditions. Nevertheless, it is important, before tracking smaller changes/degradations, to know what a complete degradation gives. Therefore, this initial experiment shows how photoelectron spectroscopy can give reliable chemical information qualitatively and quantitatively and thus validate our methodology and results obtained in the following parts.

In this context, the effect from a second parameter was investigated; the effect of time in different atmospheres on the MAPbI_3 surface structure. In this case, a perovskite sample was divided into two pieces: one part was stored in ambient air, and the second one in an argon-filled glovebox ($\text{O}_2 < 1 \text{ ppm}$, $\text{H}_2\text{O} < 1 \text{ ppm}$). Both were kept at room temperature in a dark environment and PES was carried out after 10 weeks of storage. The evolution of the I/Pb and N/Pb ratios is presented in Table 3.

The initial I/Pb and N/Pb ratios for this sample are 3.1 and 0.9. They are slightly different from the values presented in Table 1, which exhibit the difficulty in obtaining highly reproducible samples. After 10 weeks in argon, both ratios decrease by 0.2, whereas it decreases by 0.3 in air. In both cases of air and argon exposure, degradation is observed. The sensitivity to water discussed above, together with methylammonium halide sublimation, can be used as a tentative explanation when stored in air. Christians et al. recently suggested that, in darkness, H_2O in a controlled humidified atmosphere is able to complex with the perovskite, forming a similar hydrated phase: $(\text{CH}_3\text{NH}_3)_4\text{PbI}_6 \cdot 2\text{H}_2\text{O}$.⁵⁵ Nevertheless, the presence of a hydrate is not supported by our PES results, because our N/Pb and I/Pb ratios decrease in accord with the formation of PbI_2 , whereas they would increase in the presence of hydrates. Yang et al. confirmed the formation of hydrates as a first step in the decomposition process using *in situ* grazing-incidence X-ray diffraction (GIXRD) measurements in a controlled H_2O atmosphere.⁵⁶ Nevertheless, they point out that this hydrate is unstable in a room-temperature air atmosphere and MAPbI_3 is quickly reformed back. They also concluded that the further decomposition leads to the degradation of $\text{CH}_3\text{NH}_3\text{I}$ to CH_3NH_2 and HI , leaving only PbI_2 as a byproduct, in keeping with their *ex situ* XRD and our PES data. The degradation while stored in argon is slower but still present. The explanation may be more intriguing, but even if it is weak, it has a tendency to confirm the overall instability

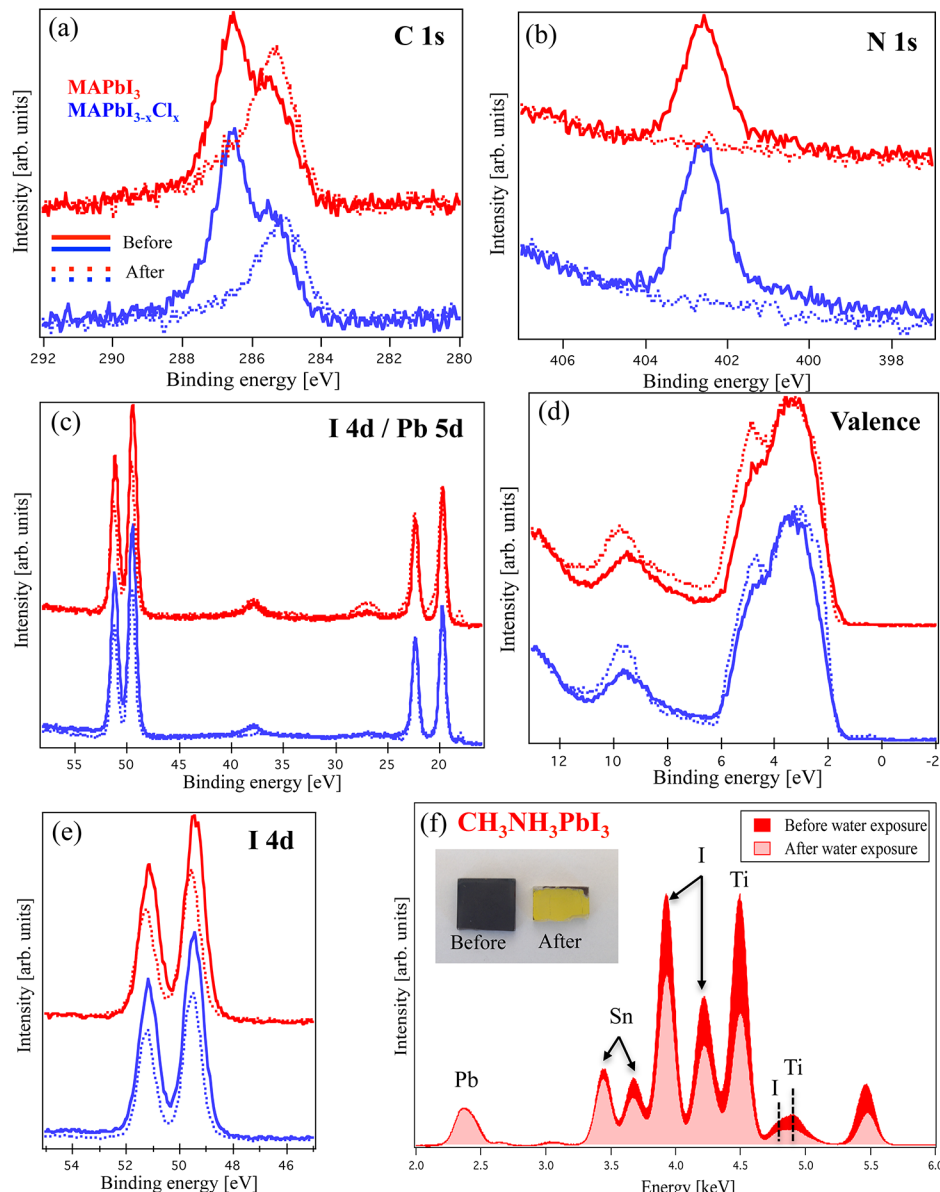


Figure 5. C 1s, N 1s, and Pb 5d/I 4d core level spectra (panels (a), (b), and (c)) and valence spectra (panel (d)) of $\text{CH}_3\text{NH}_3\text{PbI}_3$ (in red) and $\text{CH}_3\text{NH}_3\text{PbI}_{3-x}\text{Cl}_x$ (in blue) recorded with an excitation energy of 4000 eV. The solid and dotted lines correspond to the spectra before and after water exposure, respectively. (e) Enlarged view of the I 4d core level. (f) EDX spectra of the MAPbI_3 before (dark red) and after (light red) water exposure. A picture of the sample is displayed in the inset.

Table 2. I/Pb Intensity Ratio Calculated from Experimental Results of the MAPbI_3 and $\text{MAPbI}_{3-x}\text{Cl}_x$ Samples after Water Exposure

experiment	I/Pb intensity ratio
$\text{MAPbI}_3 + \text{H}_2\text{O}$	1.9
$\text{MAPbI}_{3-x}\text{Cl}_x + \text{H}_2\text{O}$	1.9

of the perovskite materials and the necessity to perform future studies to better understand the mechanism and overcome this issue.

3.4. Thermal Stability and X-ray Beam Damage on MAPbI_3 . The last materials exposure investigated is the temperature effect on the perovskite structure. The effect of the annealing temperature on the perovskite structure has been investigated recently by Dualeh et al.,³³ but we have focused on the effect of heating on already-prepared MAPbI_3 samples in an

Table 3. Evolution upon Time of the I/Pb and N/Pb Intensity Ratios Calculated from Experimental Results, Depending on the Storage Conditions

MAPbI_3	fresh (5 days)	stored 10 weeks in argon	stored 10 weeks in air
I/Pb intensity ratio	3.1	2.9	2.8
N/Pb intensity ratio	0.9	0.7	0.6

oxygen- and water-free environment. The prepared sample was heated in the analysis chamber of the spectrometer in an ultrahigh vacuum environment; thus, cross-effects with air or humidity are strictly avoided. Two sets of experiments have been performed, and special attention has been devoted to distinguish between the reactions due to temperature and those

related to X-ray beam damage. The two procedures are described in the Experimental Details section.

Figure 6 describes the evolution of the resulting I/Pb and N/Pb ratios upon the two heating procedures used. During the

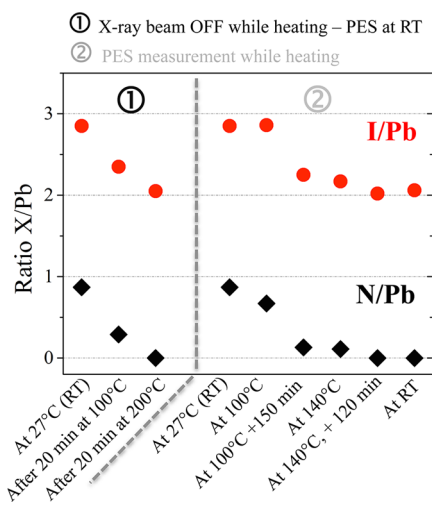
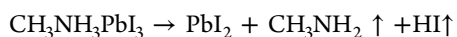


Figure 6. Evolution of the I/Pb ratio (red circle) and the N/Pb ratio (black square) during the two different heating procedures presented in the Experimental Details section.

first procedure (marked “①” in Figure 6), a potential impact induced by the X-ray beam has been removed, since the X-ray beam was switched off when the sample was heated and cooled; all the measurements were carried out at room temperature, and each time on a fresh spot. In the first step, the sample was heated to 100 °C for 20 min; the sample was then heated to 200 °C for the same time. We can note that the initial I/Pb and N/Pb ratios are lower than the theoretical ones (2.9 and 0.9, respectively, compared to 3 and 1). This is probably due to the fact that this sample was not stored in an argon-filled container and degradation might have started already (MAPbI₃:PbI₂, 85:15). The evolution of the I/Pb and N/Pb ratios are presented in Figure 6 (left part marked “①”). After 20 min at 100 °C, I/Pb and N/Pb have dropped to 2.35 and 0.3, respectively, i.e., MAPbI₃:PbI₂ ≈ 70:30. After 200 °C, the ratios are 2.0 and 0 (i.e., 100% of PbI₂). No significant increase of Pb⁰ was observed. The following mechanism can thus be suggested:³³



Those results clearly show that the MAPbI₃ perovskite starts to decompose already after a short exposure at 100 °C, which is significantly lower than the results from recent studies.^{40,41} It is important to remember that the heating in this present work was performed in a ultrahigh vacuum environment, which might explain why the perovskite degradation occurs at lower temperature than that usually reported in the literature by different techniques operating at atmospheric pressure (XRD). Tan et al. reported a similar sensitivity using *in situ* grazing-incidence wide-angle X-ray scattering (GIWAXS). Such degradation can appear as a big drawback, since the annealing temperature during the perovskite formation usually occurs in this temperature range. Therefore, the annealing time is a crucial point that needs to be long enough to form the perovskite and eliminate extra solvent, but short enough to avoid degradation of the materials.³³

For the second procedure (marked “②”), the sample was illuminated by the X-ray beam on the same spot during the entire procedure and the sample was heated to 100 °C and then to 140 °C. The sample was then cooled to room temperature.

Successive PES measurement series were done during the process. Figure 6 (right part) shows that, when the sample temperature has reached 100 °C, a small evolution is directly observed after 20 min and after 150 min, the I/Pb ratio decreased to 2.2 and the N/Pb ratio decreased to 0.1. At 140 °C, the ratios are still decreasing, finally reaching 2.0 for I/Pb and 0 for N/Pb, corresponding to a total degradation into PbI₂. These values are maintained when the sample was brought back to room temperature.

The evolution of the Pb 4f core level spectra, relative to this heating procedure, is presented in Figure 7. Before heating, a

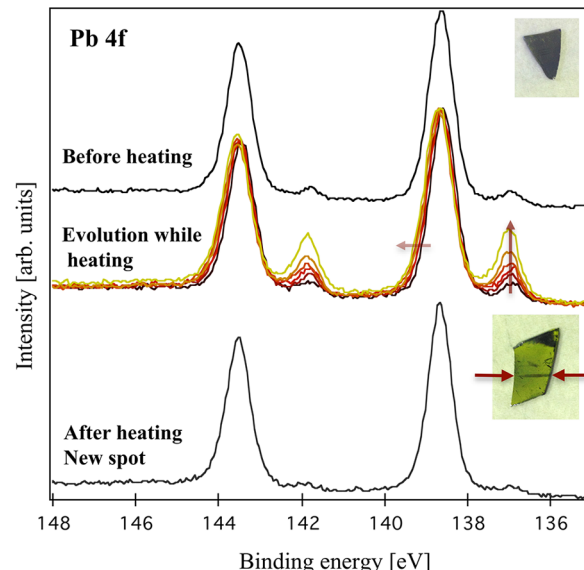
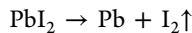


Figure 7. Evolution of the Pb 4f core level spectra of the MAPbI₃/meso-TiO₂/Si, before, during and after the first heating procedure described in Figure 5. Spectra were recorded with an excitation energy of 4000 eV. Pictures of a sample before and after the procedure are presented as insets.

main peak at 138.6 eV is observed due to the perovskite phase and a small peak at 137.0 eV assigned to Pb⁰ is also detected, as noted earlier in this paper (Figure 1). During heating, the degradation of the perovskite observed by quantification can be followed by examining the spectra. The main Pb 4f_{7/2} peak is slowly shifted toward higher binding energy (138.7 eV), in agreement with the decomposition into PbI₂. We can also note a significant intensity increase of the Pb⁰ peak at 137.0 eV while heating. This last point is only related to X-ray beam damage. Once the sample was back to room temperature, a new spot was investigated, and, in this case, the main peak presented a binding energy of 138.7 eV and the calculated ratio I/Pb was 2. The degradation to PbI₂ was thus observed all over the sample. The metallic lead is similar to the initial spectra prior heating. The picture presented in the inset in Figure 7 confirms these speculations: we can clearly see that the entire sample is yellow, but a red horizontal line is observed in the middle, corresponding to the irradiated area. Those results show that already at 100 °C, a degradation of the perovskite phase into PbI₂ occurs. Besides heating, in parallel, X-ray-induced degradation enhances the formation of Pb⁰.



4. CONCLUSIONS

Largely based on hard X-ray photoelectron spectroscopy (XPS), we have investigated the stability of methylamine lead halide perovskites and their evolution under diverse conditions, such as water exposure, as well as varying thermal treatment and time in different environments. Some support from a more bulk-sensitive technique, energy-dispersive X-ray spectroscopy, was also included. The experiments have provided valuable information regarding the chemical composition of the investigated materials.

The mixed halide usually referred to as $\text{MAPbI}_{3-x}\text{Cl}_x$ does not contain any measurable amounts of chlorine in its final form and the classical MAPbI_3 material is obtained. Identical electronic structures, in terms of core-level and valence level structure, as well as chemical compositions, are obtained for MAPbI_3 and $\text{MAPbI}_{3-x}\text{Cl}_x$. However, using PbCl_2 instead of PbI_2 in the synthesis slows the perovskite formation, resulting in different structure morphologies.

Despite different formation mechanisms, $\text{MAPbI}_{3-x}\text{Cl}_x$ and MAPbI_3 follow a similar degradation process in the presence of water, leading to the formation of PbI_2 and the disappearance of the methylamine group. A similar degradation is observed as soon as the temperature gets close to 100 °C. Finally, while humidity is often cited to explain the degradation of perovskites, we show that a slow degradation occurs even when stored in an inert atmosphere such as argon.

Various encapsulation techniques or the addition of a hole transport layer⁵⁶ have been currently suggested to avoid any humidity/water contact and can stabilize the perovskite materials; nevertheless, other approaches have to be found. Regarding the perovskite itself, the first solution would be to improve the stability of what we think is the weakest point: the organic part. Substitution of a part of the methylammonium group could improve the overall stability.¹⁴ Also, the annealing procedure is critical, and without perfect control of the temperature, it is very difficult to get reproducible solar cells. Low-temperature solution processes have been reported.¹⁸

AUTHOR INFORMATION

Corresponding Authors

*E-mail: bertrand.philippe@physics.uu.se (B. Philippe).

*E-mail: hakan.rensmo@physics.uu.se (H. Rensmo).

Notes

The authors declare no competing financial interest.

ACKNOWLEDGMENTS

We acknowledge financial support from the Swedish Research Council, the Swedish Energy Agency, and StandUP for Energy. The research leading to these results has received also funding from the European Community's Seventh Framework Programme (No. FP7/2007-2013) under Grant Agreement No. 312284. Finally, HZB is acknowledged for the allocation of synchrotron radiation beamtime and especially Mihaela Gorgoi for her support.

REFERENCES

- (1) Park, N.-G. *J. Phys. Chem. Lett.* **2013**, *4*, 2423.
- (2) Hodes, G. *Science* **2013**, *342*, 317.
- (3) Green, M. A.; Ho-Baillie, A.; Snaith, H. J. *Nat. Photonics* **2014**, *8*, 506.
- (4) Grätzel, M. *Nat. Mater.* **2014**, *13*, 838.
- (5) Kojima, A.; Teshima, K.; Shirai, Y.; Miyasaka, T. *J. Am. Chem. Soc.* **2009**, *131*, 6050.
- (6) Kim, H. S.; Lee, C. R.; Im, J. H.; Lee, K. B.; Moehl, T.; Marchioro, A.; Moon, S. J.; Humphry-Baker, R.; Yum, J. H.; Moser, J. E.; Grätzel, M.; Park, N. G. *Sci. Rep.* **2012**, *2*, 591.
- (7) Lee, M. M.; Teuscher, J.; Miyasaka, T.; Murakami, T. N.; Snaith, H. J. *Science* **2012**, *338*, 643–647.
- (8) Burschka, J.; Pellet, N.; Moon, S.-J.; Humphry-Baker, R.; Gao, P.; Nazeeruddin, M. K.; Grätzel, M. *Nature* **2013**, *499*, 316.
- (9) Liu, M.; Johnston, M. B.; Snaith, H. J. *Nature* **2013**, *501*, 395.
- (10) Jeon, N. J.; Noh, J. H.; Yang, W. S.; Kim, Y. C.; Ryu, S.; Seo, J.; Seok, S. I. *Nature* **2015**, *517*, 476–480 (DOI: 10.1038/nature14133).
- (11) Schmidt, L. C.; Pertegás, A.; González-Carrero, S.; Malinkiewicz, O.; Agouram, S.; Minguez Espallargas, G.; Bolink, H. J.; Galian, R. E.; Pérez-Prieto, J. *J. Am. Chem. Soc.* **2014**, *136*, 850.
- (12) Noh, J. H.; Im, S. H.; Heo, J. H.; Mandal, T. N.; Seok, S. I. *Nano Lett.* **2013**, *13*, 1764.
- (13) Ogomi, Y.; Morita, A.; Tsukamoto, S.; Saitho, T.; Fujikawa, N.; Shen, Q.; Toyoda, T.; Yoshino, K.; Pandey, S. S.; Ma, T.; Hayase, S. *J. Phys. Chem. Lett.* **2014**, *5*, 1004.
- (14) Mei, A.; Li, X.; Liu, L.; Ku, Z.; Liu, T.; Rong, Y.; Xu, M.; Hu, M.; Chen, J.; Yang, Y.; Grätzel, M.; Han, H. *Science* **2014**, *345*, 295.
- (15) Eperon, G. E.; Stranks, S. D.; Menelaou, C.; Johnston, M. B.; Herz, L. M.; Snaith, H. J. *Energy Environ. Sci.* **2014**, *7*, 982.
- (16) Liu, M.; Johnston, M. B.; Snaith, H. J. *Nature* **2013**, *501*, 395.
- (17) You, J.; Hong, Z.; Yang, Y.; Chen, Q.; Cai, M.; Song, T.-B.; Chen, C.-C.; Lu, S.; Liu, Y.; Zhou, H.; Yang, Y. *ACS Nano* **2014**, *8*, 1674.
- (18) Yella, A.; Heiniger, L. P.; Gao, P.; Nazeeruddin, M. K.; Grätzel, M. *Nano Lett.* **2014**, *14*, 2591.
- (19) Chen, Q.; Zhou, H.; Hong, Z.; Luo, S.; Duan, H.-S.; Wang, H.-H.; Liu, Y.; Li, G.; Yang, Y. *J. Am. Chem. Soc.* **2014**, *136*, 622.
- (20) Gao, P.; Grätzel, M.; Nazeeruddin, M. K. *Energy Environ. Sci.* **2014**, *7*, 2448.
- (21) Kim, H. S.; Im, S. H.; Park, N.-G. *J. Phys. Chem. C* **2014**, *118*, 5615.
- (22) Oga, H.; Saeki, A.; Ogomi, Y.; Hayase, S.; Seki, S. *J. Am. Chem. Soc.* **2014**, *136*, 13818.
- (23) Leijtens, T.; Stranks, S. D.; Eperon, G. E.; Lindblad, R.; Johansson, E. M. J.; McPherson, I. J.; Rensmo, H.; Ball, J. M.; Lee, M. M.; Snaith, H. J. *ACS Nano* **2014**, *8*, 7147.
- (24) Juarez-Perez, E. J.; Wußler, M.; Fabregat-Santiago, F.; Lakus-Wollny, K.; Mankel, E.; Mayer, T.; Jaegermann, W.; Mora-Sero, I. *J. Phys. Chem. Lett.* **2014**, *5*, 680.
- (25) Gonzalez-Pedro, V.; Juarez-Perez, E. J.; Arsyad, W.-S.; Barea, E. M.; Fabregat-Santiago, F.; Mora-Sero, I.; Bisquert, J. *Nano Lett.* **2014**, *14*, 888.
- (26) Edri, E.; Kirmayer, S.; Henning, A.; Mukhopadhyay, S.; Gartsman, K.; Rosenwaks, Y.; Hodes, G.; Cahen, D. *Nano Lett.* **2014**, *14*, 1000.
- (27) Mosconi, E.; Ronca, E.; De Angelis, F. *J. Phys. Chem. Lett.* **2014**, *5*, 2619.
- (28) Lindblad, R.; Bi, D.; Park, B.-W.; Oscarsson, J.; Gorgoi, M.; Siegbahn, H.; Odelius, M.; Johansson, E. M. J.; Rensmo, H. *J. Phys. Chem. Lett.* **2014**, *5*, 648.
- (29) Park, B.-W.; Philippe, B.; Gustafsson, T.; Sveinbjörnsson, K.; Hagfeldt, A.; Johansson, E. M. J.; Boschloo, G. *Chem. Mater.* **2014**, *26*, 4466.
- (30) Colella, S.; Mosconi, E.; Fedeli, P.; Listorti, A.; Gazza, F.; Orlando, F.; Ferro, P.; Besagni, T.; Rizzo, A.; Calestani, G.; Gigli, G.; De Angelis, F.; Mosca, R. *Chem. Mater.* **2013**, *25*, 4613.
- (31) Colella, S.; Mosconi, E.; Pellegrino, G.; Alberti, A.; Guerra, V. L. P.; Masi, S.; Listorti, A.; Rizzo, A.; Condorelli, G. G.; De Angelis, F.; Gigli, G. *J. Phys. Chem. Lett.* **2014**, *5*, 3532.
- (32) Edri, E.; Kirmayer, S.; Kulbak, M.; Hodes, G.; Cahen, D. *J. Phys. Chem. Lett.* **2014**, *5*, 429.
- (33) Dualeh, A.; Tétreault, N.; Moehl, T.; Gao, P.; Nazeeruddin, M. K.; Grätzel, M. *Adv. Funct. Mater.* **2014**, *24*, 3250.

- (34) Yu, H.; Wang, F.; Xie, F.; Li, W.; Chen, J.; Zhao, N. *Adv. Funct. Mater.* **2014**, *24*, 7102.
- (35) Unger, E. L.; Bowring, A. R.; Tassone, C. J.; Pool, V.; Gold-Parker, A.; Checharoen, R.; Stone, K. H.; Hoke, E. T.; Toney, M. F.; McGehee, M. D. *Chem. Mater.* **2014**, *26*, 7158.
- (36) Dar, M. I.; Arora, N.; Gao, P.; Ahmad, S.; Grätzel, M.; Nazeeruddin, M. K. *Nano Lett.* **2014**, *14*, 6991.
- (37) Mosconi, E.; Amat, A.; Nazeeruddin, M. K.; Grätzel, M.; De Angelis, F. *J. Phys. Chem. C* **2013**, *117*, 13902.
- (38) Schultz, P.; Edri, E.; Kirmayer, S.; Hodes, G.; Cahen, D.; Kahn, A. *Energy Environ. Sci.* **2014**, *7*, 1377.
- (39) Tan, K. W.; Moore, D. T.; Saliba, M.; Sai, H.; Estroff, L. A.; Hanrath, T.; Snaith, H. J.; Wiesner, U. *ACS Nano* **2014**, *8*, 4730.
- (40) Pistor, P.; Borchert, J.; Fränzel, W.; Csuk, R.; Scheer, R. *J. Phys. Chem. Lett.* **2014**, *5*, 3308.
- (41) Supasai, T.; Rujisamphan, N.; Ullrich, K.; Chemseddine, A.; Dittrich, T. *Appl. Phys. Lett.* **2013**, *103*, 183906.
- (42) Kim, H.-S.; Lee, C.-R.; Im, J.-H.; Lee, K.-B.; Moehl, T.; Marchioro, A.; Moon, S.-J.; Humphry-Baker, R.; Yum, J.-H.; Moser, J. E.; Grätzel, M.; Park, N.-G. *Sci. Rep.* **2012**, *2*, 591.
- (43) Schaefers, F.; Merlin, M.; Gorgoi, M. *Rev. Sci. Instrum.* **2007**, *78*, 123102.
- (44) Gorgoi, M.; Svensson, S.; Schäfers, F.; Öhrwall, G.; Mertin, M.; Bressler, P.; Karis, O.; Siegbahn, H.; Sandell, A.; Rensmo, H.; Doherty, W.; Jung, C.; Braun, W.; Eberhardt, W. *Nucl. Instrum. Methods Phys. Res., Sect. A* **2009**, *601*, 48.
- (45) Scofield, J. H. *J. Electron Spectrosc. Relat. Phenom.* **1976**, *8*, 129.
- (46) Eperon, G. E.; Burlakov, V. M.; Docampo, P.; Goriely, A.; Snaith, H. J. *Adv. Funct. Mater.* **2014**, *24*, 151.
- (47) Bass, K. B.; McAnally, E.; Zhou, S.; Djurovich, P. I.; Thompson, M. E.; Melot, B. C. *Chem. Commun.* **2014**, *50*, 15819.
- (48) Williams, S. T.; Zuo, F.; Chueh, C.-C.; Liao, C.-Y.; Liang, P.-W.; Jen, A. K.-Y. *ACS Nano* **2014**, *8*, 10640–10654 (DOI: 10.1021/nn5041922).
- (49) Tidhar, Y.; Edri, E.; Weissman, H.; Zohar, D.; Hodes, G.; Cahen, D.; Rybtchinski, B.; Kirmayer, S. *J. Am. Chem. Soc.* **2014**, *136*, 13249.
- (50) Conings, B.; Baeten, L.; De Dobbelaere, C.; D'Haen, J.; Manca, J.; Boyen, H.-G. *Adv. Mater.* **2014**, *26*, 2041.
- (51) Westermark, K.; Henningsson, A.; Rensmo, H.; Södergren, S.; Siegbahn, H.; Hagfeldt, A. *Chem. Phys.* **2002**, *285*, 157.
- (52) Kitazawa, N.; Watanabe, Y.; Nakamura, Y. *J. Mater. Sci.* **2002**, *14*, 3585.
- (53) Moulder, J. F.; Stickle, W. F.; Sobol, P. E.; Bomben, K. D. *Handbook of X-ray Photoelectron Spectroscopy*; Physical Electronics, Inc.: Eden Prairie, MN, 1995 (ISBN: 0-9648124-1-X).
- (54) Conings, B.; De Dobbelaere, C.; D'Haen, J.; Van Bael, M. K.; Manca, J.; Boyen, H.-G. *HOPV14* **2014**, 079.
- (55) Christians, J. A.; Miranda Herrera, P. A.; Kamat, P. V. *J. Am. Chem. Soc.* **2015**, *137*, 1530.
- (56) Yang, J.; Siempelkamp, B. D.; Liu, D.; Kelly, T. L. *ACS Nano* **2015**, DOI: 10.1021/nn506864k.